

A unified model for long-period radio transients and white dwarf binary pulsars

Csanád Horváth¹, Nanda Rea^{2,3}, Natasha Hurley-Walker¹, Samuel J. McSweeney¹, Richard A. Perley⁴, Emil Lenc⁵

¹*International Centre for Radio Astronomy Research, Curtin University, Kent St, Bentley WA 6102, Australia*

²*Institute of Space Sciences (ICE, CSIC), Campus UAB, Carrer de Can Magrans s/n, 08193, Barcelona, Spain*

³*Institut d'Estudis Espacials de Catalunya (IEEC), Esteve Terradas 1, RDIT Building, 08860, Castelldefels, Spain*

⁴*National Radio Astronomy Observatory, Socorro, NM 87801, USA*

⁵*Australia Telescope National Facility, CSIRO, Space & Astronomy, Epping, New South Wales, Australia*

Long-period radio transients (LPTs) represent a recently uncovered class of Galactic radio sources exhibiting minute-to-hour periodicities and highly polarised pulses of second-to-minute duration. Their phenomenology does not fit exactly in any other class, although it might resemble that of radio magnetars or of white dwarf (WD) radio emitting binary systems. Notably, two LPTs with confirmed multi-wavelength counterparts have been identified as synchronised white dwarf–M dwarf binaries (polars). Meanwhile, systems such as AR Scorpii and J1912–44 exhibit short-period pulsations in a hr-tight orbit, with polarized

radio emission proposed to be generated by the interaction of the WD magnetosphere with the low-mass companion wind.

Here we demonstrate that both LPTs and WD binary pulsars can be explained within a single geometric model in which radio emission is triggered when the magnetic pole of a rotating white dwarf intersects its companion’s wind in the binary orbital plane. We use a 36-year timing baseline to infer the orbital period and binary geometry solely from radio data of GPM J1839–10, the longest-active LPT known. The model naturally predicts its intermittent emission and double-pulse structure. Crucially, we show that the beat period between the spin and the orbit matches the observed pulse substructure and polarisation signatures, providing strong support for the model. Applying this model to the WD binary pulsar J1912–44 it can also reproduce the system emission and geometry. Our results place GPM J1839–10, and other LPTs in general and radio emitting WD binaries, at different stages of a continuum between intermediate and synchronised polars, suggesting a unified population of magnetic WD binaries driving coherent radio emission.

White dwarf binary systems are increasingly recognised as hosts of exotic pulsar-like emission, challenging long-standing assumptions that coherent radio pulses are exclusive to neutron star systems^{1,2}. The discovery of long-period transients (LPTs), characterised by long periodicities (minutes to hours) , and strong polarisation, further deepens the mystery of how and where coherent radio emission originates^{3,4}. These intriguing systems are characterized by periodic radio pulses with high polarization (both linear and circular) and a high surface brightness pointing to a coherent radio emission process. However, the luminosities of the bright radio pulses in the ~ 10

systems discovered thus far, exceed their rotational power, leaving uncertain the energy source. A strong magnetic field has been suggested to overcome this energy problem, suggesting at first the possibility of them being radio magnetars having perhaps had large fall-back at birth slowing down their periods ^{5,6}.

Two LPTs, ILT J1101+5521 ⁷ and GLEAM-X J0704-37 ^{8,9}, have recently been associated with a WD-M dwarf binary system via the detection of the orbital motion in the optical spectrum of the M companion star, at a period coincident with the radio pulse period. These systems might be hosting a WD with a spin synchronized with the orbital motion, hence belonging to the class of polars, despite not being in an accretion phase. In contrast, the AR Scorpii (Ar Sco) and J1912-44 radio emitting binary WDs are not synchronised with their companions; coherent radio pulses are observed at beat periods resulting from the interaction between the white dwarf spin and the orbital motion. The radio emission in these systems has been intriguing all along, and scenarios involving the dipolar losses of the white dwarf rotating field and the interaction with the M-dwarf companion wind have been proposed ¹⁰⁻¹²

The phenomenological similarities between these sources invite a unified physical framework. We propose a geometric emission model in which radiation is generated when a WD's magnetic pole sweeps across its companion star, injecting relativistic particles from the M dwarf's wind into the WD's magnetosphere ^{13,14}. These particles are accelerated along magnetic field lines, producing a collimated radio beam aligned with the magnetic moment of the WD. The model incorporates orbital inclination, magnetic obliquity, and beam geometry, and predicts observable

intensity variations as a function of the spin and orbital phase. Further intensity variations observed in the long-term radio outbursts of LPTs might be ascribed to the intrinsic variability of the M-dwarf wind.

Our model assumes a circular orbit with inclination angle i between the orbital axis and the WD spin axis. The magnetic moment is tilted by angle α from the spin axis, and maximum radio emission is generated in the direction of the magnetic moment. Emission is modulated in two ways: (1) by the angle β_{MD} between the magnetic pole and the M dwarf, governing the availability of particles via an assumed Gaussian function; and (2) by the angle β between the magnetic pole and the Earth, determining visibility to observers. This model, although simplified, provides predictive power: emission is expected when both β_{MD} and β are small. The resulting phase-space of emission naturally leads to double-peaked pulse groups and intermittent visibility consistent with observations.

GPMJ1839–10 is the longest lived LPT known, exhibiting a 22-minute period with sporadic pulses observed across 36 years of archival radio data ⁴. In a coordinated campaign using MeerKAT, ASKAP, and VLA in 2024, we identified a higher-order periodicity: pulses cluster in double groups occurring every ~ 8.75 hr. We interpret this as the orbital period $T = 31482.4 \pm 0.2$ s, which we are able to measure to such low uncertainty by taking advantage of the 36 year baseline.

Folding the data over this 8.75 hr modulation period and the previously reported 22-minute period (P_A)⁴, as well as the derived beat period (P_B), reveals in [Figure 1](#) that the pulse substructure aligns between pulses with $P_B = 1265.2197 \pm 0.0002$ s, rather than $P_A = 1318.1957 \pm 0.0002$

s. The substructure timescale of ~ 50 s is consistent throughout the archival data, first discovered by autocorrelation between pulses ⁴, and folding on P_B reveals further correlation and vertical alignment of the brightest peaks. This suggests that P_B corresponds to the true spin period of the white dwarf (while P_A is a spin-orbit beat period) inviting its interpretation as the cross-section of the radio beam.

The phase difference between the left and right pulse groups cannot be attributed to the difference in light travel time between orbital phases because that would be on the order of seconds for an orbit of this size, not minutes. Instead, we interpret the groups as arising from the intersections of the M dwarf's highly inclined orbit with the cone traced out by the WD's magnetic pole. This explains both the intermittency and the phase delay between pulse groups. Our geometric model reproduces the observed dynamic pulse profile as shown in [Figure 2](#) when fitted using a Markov chain Monte Carlo method, with best-fit parameters indicating a near-perpendicular orbital inclination $i = 100.1 \pm 0.6^\circ$. The modelled pulse groups are the regions where the β_{MD} contours cut into the central column of the β colour map — where the Earth, MD, and WD pole are sufficiently aligned. No good fit exists for P_A as the spin period.

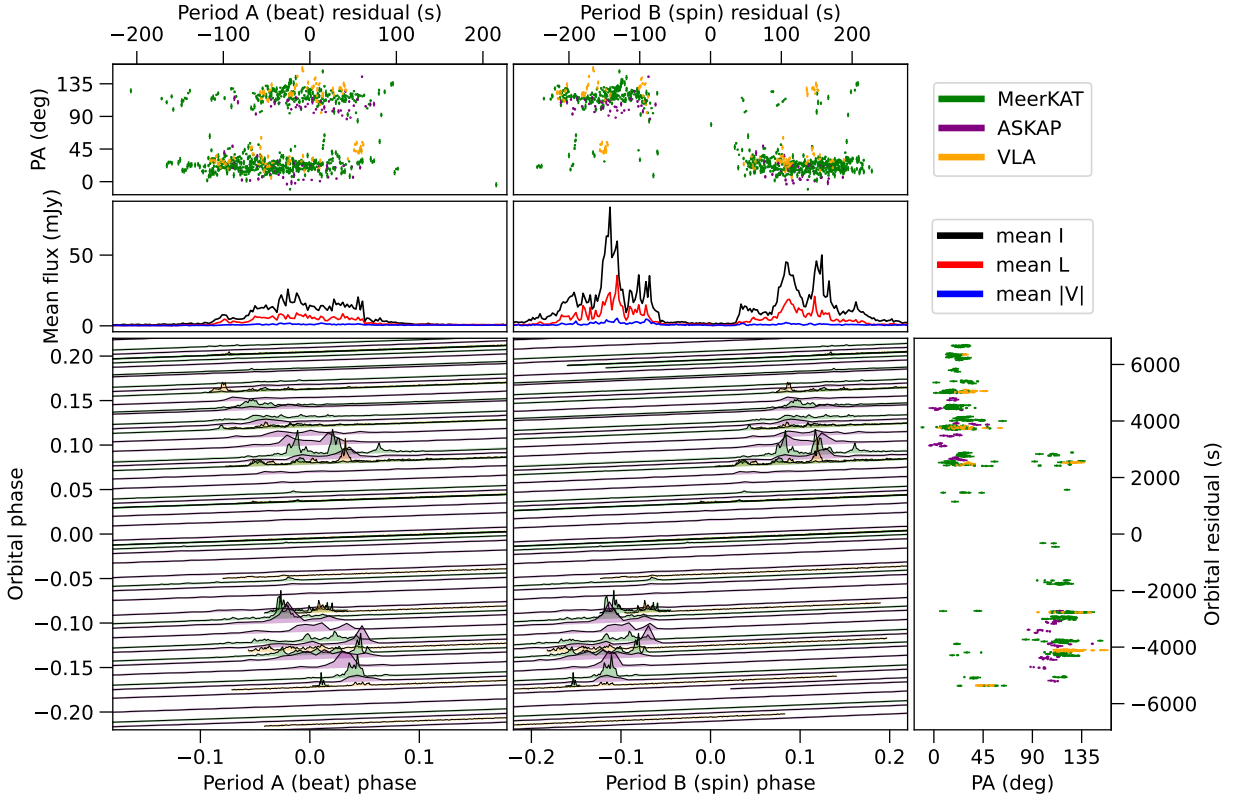


Figure 1: Dynamic pulse profile and polarisation position angles of GPM J1839–10. Profiles are folded vertically on the orbital period $T = 31482.4 \pm 0.2$ s and horizontally on $P_A = 1318.1957 \pm 0.0002$ s (left) and $P_B = 1265.2197 \pm 0.0002$ s (right). Above, the mean flux is calculated over two boxes enclosing the pulse groups: $\{-0.18 < \text{orbital phase} < 0.18\}$ for period A, $(\{-0.18 < \text{orbital phase} < -0.06\} \cap \{\text{spin phase} < 0\}) \cup (\{0.06 < \text{orbital phase} < 0.18\} \cap \{\text{spin phase} > 0\})$ for period B.

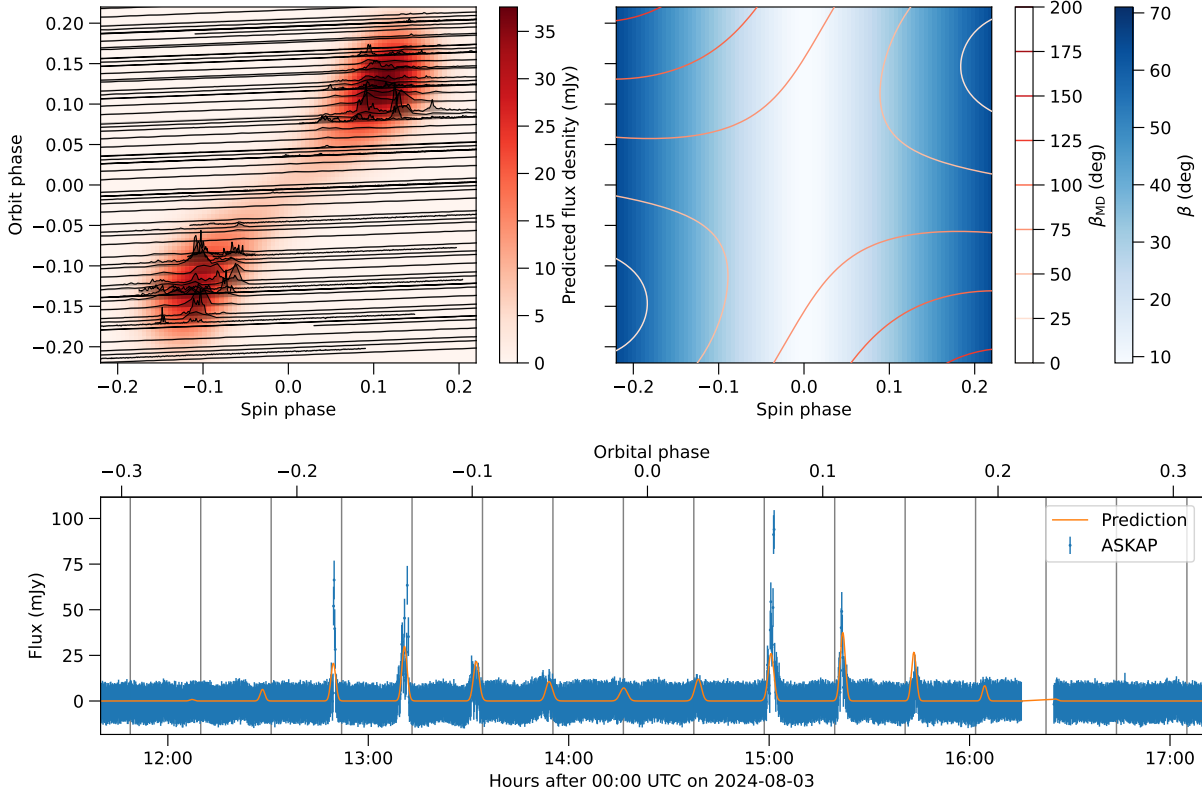


Figure 2: Modelled dynamic pulse profile of GPM J1839–10. At top left, the flux density predicted by the model I_{pred} using the best-fit parameters found using MCMC is overlaid on the real pulse profiles. At top right, the colourmap is the LOS-beam angle β as a function of spin-orbit phase, and the contours are the beam-MD angle β_{MD} . I_{pred} is greatest where β and β_{MD} are the smallest. The bottom panel is a full orbit recorded by ASKAP and the associated model prediction. The vertical lines are spaced by the spin period.

The emission is consistently highly linearly polarised with occasional 90° jumps in polarisation angle (PA) to orthogonal polarisation modes (OPMs)⁴. However, [Figure 1](#) reveals that the two

pulse groups which appear at different orbital and spin phases are dominated by different OPMs, with a similar amount of variation in each group ($\sigma_{\text{PA}} \approx \sim 10^\circ$). The PAs of individual pulses, however, may evolve more gradually and systematically across spin phase¹⁵ than can be seen in the point clusters in the figure. It can further be seen that there is a small downturn in the PAs at around spin phase -0.05 (the trailing edge of the first group), as well as a similar upturn in the PAs at spin phase 0.05 (the leading edge of the second group). Despite the possibility that pulses arriving between the two groups could potentially connect the PAs smoothly across intermediate spin/orbital phases, the flatness of the PAs of the two groups themselves, as well as the occasional 90° jump within each group, lead us to prefer an OPM interpretation over a rotating vector model one¹⁶.

Although not well understood, OPMs in pulsars are thought to be magnetospheric in origin, possibly due to birefringent properties of the co-rotating plasma¹⁷. We advance a similarly broad interpretation here: the OPMs are dominated by the average magnetic properties of the plasma through which the WD beam propagates along our line of sight. The consistency with which each pulse group exhibits the same dominant OPM support our geometric model, with the line of sight intersecting different physical sections of the intrabinary magnetic field during the two pulse groups. Both the single pulse PA variations and the occasional OPM jump even within a pulse group may be due to turbulence in the intrabinary wind.

Other spectral characteristics (dispersion measure, rotation measure, spectral shape) remain constant across the orbit, suggesting that variability arises primarily from geometric effects rather

than intrinsic source changes on a short timescale, or propagation effects. On longer timescales (a few orbits) variability is primarily driven by MD wind activity.

To describe the system geometry, we place the WD at the origin with \hat{z} as the WD spin axis, and the orbital axis inclined about \hat{y} . Fitting the model for GPMJ1839–10, we find an orbital inclination $i = 100.1 \pm 0.6^\circ$ and magnetic obliquity $\alpha = 52.1 \pm 0.4^\circ$ with respect to \hat{z} . Our line of sight has azimuth $\phi_0 = 179.29 \pm 0.04^\circ$ measured from \hat{x} and zenith $\zeta = 61 \pm 2^\circ$ measured from \hat{z} . The radio beam has an opening angle of $W_{\text{spin}} = 65 \pm 3^\circ$ and becomes active when the MD is within $W_{\text{orb}} = 70 \pm 1^\circ$ of the WD magnetic moment $\hat{\mu}$. In [Figure 3](#) we show the derived beam angle and orbit of the system together with critical radii to understand the emission state of the binary. The derived orbital period and WD spin period imply that: 1) the whole system is inside the WD light cylinder, 2) the companion star, if assumed to be an M-dwarf (as for the other two LPTs), is not filling its Roche-Lobe, and 3) depending on the assumed M-dwarf mass loss rate ($\sim 10^{-14} M_\odot \text{ yr}^{-1}$ [18](#)), the WD Alfvén radius might be inside the corotation radius, implying that during stellar flares the system may undergo accretion episodes (possibly showing transient X-ray emission as observed in the LPT ASKAPJ1832-0911 [19](#)), while being in propeller most of the time [14,20](#). Furthermore, the system geometry clearly shows how the rotating WD magnetosphere is naturally engulfed by the MD wind, possibly being the seed particles that are accelerated by the sweeping magnetic field lines generating the pulsed synchrotron radio emission [21–23](#).

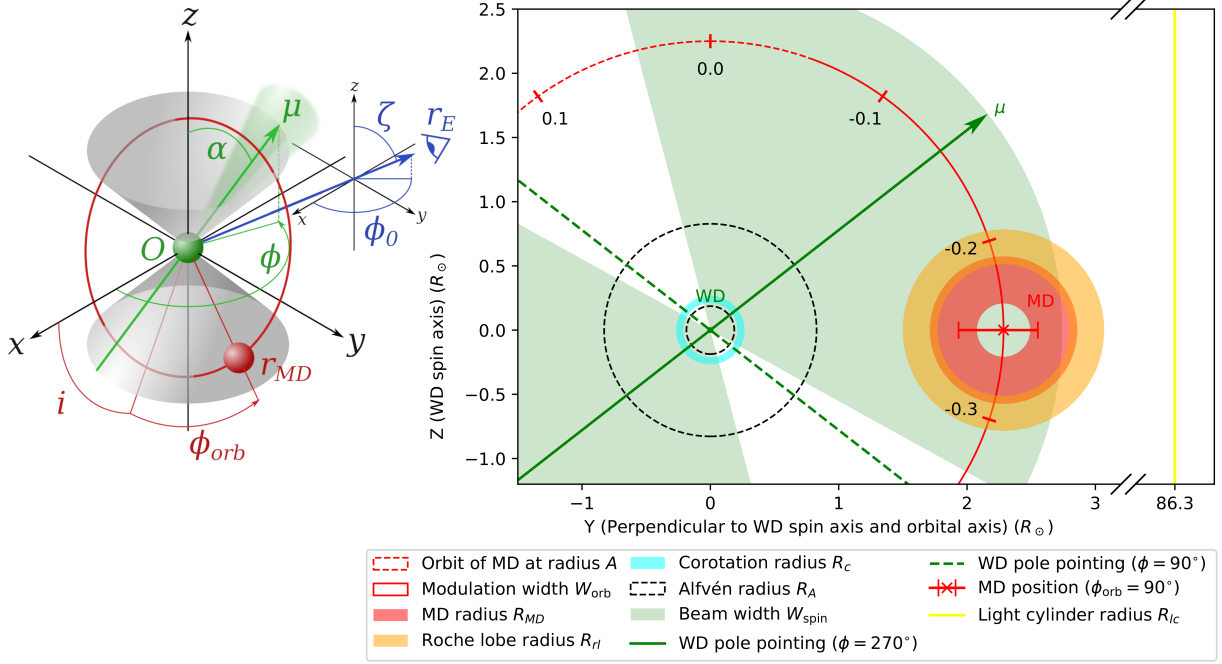


Figure 3: Diagram of the binary system, in a moving reference frame centred on the WD. At left is a not-to-scale diagram of the geometric parameters. In green is WD with its magnetic moment vector. In red, the MD with its orbital path. The blue vector points towards Earth. At right is a to-scale projection of GPMJ1839–10 on the y - z plane, with orbital phases marked. The cone traced by $\hat{\mu}$ crosses the y - z plane at the green full and dashed lines. The shaded red, orange, and cyan regions cover the ranges of R_{MD} , R_{rl} , and R_c respectively, given the MD mass is $M_{MD} \in [0.14, 0.5]M_{\odot}$ and the WD mass is $M_{WD} \in [0.6, 1.2]M_{\odot}$. The green sector and solid red line are W_{spin} and W_{orb} respectively. The small and large black dashed circles are the Alfvén radii for the minimum and maximum WD masses respectively, assuming a stellar mass loss rate of $\dot{M}_{MD} = 10^{-14} M_{\odot} \text{ yr}^{-1}$ ¹⁸.

To test the generality of the model, we applied it to 7.5 hours of MeerKAT observations of the WD binary pulsar J1912–44. Folding the data over the 5.3 minute spin and 4.03 hour orbital periods ² forms the vertically aligned dynamic pulse profile in Figure 6. We used a prior of $i = 59 \pm 6^\circ$ based on the inclination angle constraints as measured in the optical band ¹⁴. Given the prior, we find the following constraints on the geometry: $i \in [53, 65]^\circ$, $\alpha \in [42, 70]^\circ$, $\phi_0 \in [-48, -17]^\circ$, $\zeta \in [39, 73]^\circ$, $W_{\text{spin}} \in [20, 60]^\circ$, and $W_{\text{orb}} \in [67, 90]^\circ$. These results agree broadly with the earlier proposed geometry ¹⁴, but with only one pulse group the geometrical parameters are less constrained than for GPM J1839–10.

A critical component of the model is that the direction of the radio beam is locked to the WD rotating frame in the direction of the magnetic moment. If this is not the case it becomes difficult to explain the paired pulse group morphology, and it becomes unclear why the pulse substructure would be related to the spin phase. This is difficult to reconcile with models which place the emission site at or near the companion like the electron cyclotron maser emission (ECME) model ²⁴ proposed for ILT J1101+5521 or the bow shock model ¹² proposed for AR Sco. One scenario which allows for an emission region locked to the WD involves relativistic electrons accelerating from the companion towards the WD along the closed magnetic field lines when the companion star’s surface is heated by magnetic interaction ^{23,25}. The electrons emit synchrotron radiation as they reach magnetic mirror points on their way to the WD pole ²³. This idea has been shown to reproduce the dynamic pulse profile of Ar Sco with spin and orbit modulated components similar to our model ¹⁰.

In any case, the emission mechanism must differ substantially from the common radio pulsar curvature radiation process, a testable prediction of which is the beam opening angle confined by the last open field lines at the pole. Assuming that the emission site is within the orbital radius ($r_{em} \leq A \leq 2.55R_{\odot}$) places a generous limit on the half-opening angle of $\rho \leq 15^{\circ}$, inconsistent with the best-fit half-opening angle $W_{\text{spin}} = 65 \pm 3^{\circ}$. Further separating GPMJ1839–10 from neutron stars is the lack of PA sweep typically associated with the rotating vector model, although this is not a unifying feature of WD pulsars ²⁶.

Future work will include applying the model to the growing number of LPTs, which will not only test it, but serve to constrain the distribution of their geometries. Of particular interest is the 6.45 h LPT ASKAPJ183950.5–075635.0 ²⁷ which has timing variation and pulse profile evolution phenomenologically similar to GPMJ1839–10 but with an interpulse, extending the geometric parameter space. Also of interest would be J1755–2527, recently confirmed to be a 1.16 hour intermittent LPT ²⁸, the emission-state-switching 54 minute LPT ASKAPJ1935+2148 ²⁹ and CHIME J0630+25 ³⁰, whose 421 s period makes it an interesting counterpart to J1912–44.

Our results demonstrate that LPTs like GPMJ1839–10 can be understood within the same emission geometry framework as radio emitting WD binary pulsars such as J1912–44 and AR Sco. The diversity in the observed periods, pulse morphologies, and polarisation states arises from variations in orbital synchronisation and viewing geometry. This implies that coherent radio emission from magnetic WD binaries is more common and varied than previously thought, potentially forming a new class of compact binary radio emitters. However, the possible evolutionary con-

nection between these systems remains debated, and we cannot exclude them being at different evolutionary stages but with common properties and geometries allowing them to emit bright polarized radio emission. With enough samples, we expect their evolutionary stages to emerge, and the tools developed in this work will enable insight into binary WD and magnetic field evolution in a way difficult to select from optical surveys alone.

1. Buckley, D. A. H., Meintjes, P. J., Potter, S. B., Marsh, T. R. & Gänsicke, B. T. Polarimetric evidence of a white dwarf pulsar in the binary system AR Scorpii. *Nature Astronomy* **1**, 0029 (2017).
2. Pelisoli, I. *et al.* A 5.3-min-period pulsing white dwarf in a binary detected from radio to x-rays. *Nature Astronomy* **7**, 931–942 (2023).
3. Hurley-Walker, N. *et al.* A radio transient with unusually slow periodic emission. *Nature* **601**, 526–530 (2022).
4. Hurley-Walker, N. *et al.* A long-period radio transient active for three decades. *Nature* **619**, 487–490 (2023).
5. Ronchi, M., Rea, N., Graber, V. & Hurley-Walker, N. Long-period Pulsars as Possible Outcomes of Supernova Fallback Accretion. *Astrophys. J.* **934**, 184 (2022).
6. Gençali, A. A., Ertan, Ü. & Alpar, M. A. Evolution of the long-period pulsar gleam-x j162759. 5–523504.3. *Monthly Notices of the Royal Astronomical Society: Letters* **513**, L68–L71 (2022).

7. de Ruiter, I. *et al.* Sporadic radio pulses from a white dwarf binary at the orbital period. *Nature Astronomy* 1–13 (2025).
8. Hurley-Walker, N. *et al.* A 2.9 hr periodic radio transient with an optical counterpart. *The Astrophysical Journal Letters* **976**, L21 (2024).
9. Rodriguez, A. C. Spectroscopic detection of a 2.9-hour orbit in a long-period radio transient. *A&A* **695**, L8 (2025).
10. Potter, S. B. & Buckley, D. A. H. Time series photopolarimetry and modelling of the white dwarf pulsar in ar scorpii. *Monthly Notices of the Royal Astronomical Society* **481**, 2384–2392 (2018).
11. Qu, Y. & Zhang, B. Magnetic interactions in white dwarf binaries as mechanism for long-period radio transients. *The Astrophysical Journal* **981**, 34 (2025).
12. Geng, J.-J., Zhang, B. & Huang, Y.-F. A model of white dwarf pulsar ar scorpii. *The Astrophysical Journal Letters* **831**, L10 (2016).
13. Schreiber, M. R., Belloni, D., Gänsicke, B. T., Parsons, S. G. & Zorotovic, M. The origin and evolution of magnetic white dwarfs in close binary stars. *Nature Astronomy* **5**, 648–654 (2021).
14. Pelisoli, I. *et al.* Unveiling the white dwarf in J191213.72 - 441045.1 through ultraviolet observations. *MNRAS* **527**, 3826–3836 (2024).

15. Men, Y., McSweeney, S., Hurley-Walker, N., Barr, E. & Stappers, B. A highly magnetized long-period radio transient exhibiting unusual emission features. *Science Advances* **11**, eadp6351 (2025).
16. Radhakrishnan, V. & Cooke, D. J. Magnetic Poles and the Polarization Structure of Pulsar Radiation. *Astrophys. J. Lett.* **3**, 225 (1969).
17. Gangadhara, R. T. Orthogonal polarization mode phenomenon in pulsars. *A&A* **327**, 155–166 (1997).
18. Wood, B. E., Müller, H. R., Zank, G. P., Linsky, J. L. & Redfield, S. New Mass-Loss Measurements from Astrospheric Ly α Absorption. *ApJ* **628**, L143–L146 (2005).
19. Wang, Z. *et al.* Detection of X-ray Emission from a Bright Long-Period Radio Transient. *Nature* (2025).
20. Lyutikov, M. *et al.* Magnetospheric interaction in white dwarf binaries AR Sco and AE Aqr. *arXiv e-prints* arXiv:2004.11474 (2020).
21. Geng, J.-J., Zhang, B. & Huang, Y.-F. A Model of White Dwarf Pulsar AR Scorpii. *ApJ* **831**, L10 (2016).
22. Katz, J. I. AR Sco: A Precessing White Dwarf Synchronar? *ApJ* **835**, 150 (2017).
23. Takata, J., Yang, H. & Cheng, K. A model for ar scorpii: emission from relativistic electrons trapped by closed magnetic field lines of magnetic white dwarfs. *The Astrophysical Journal* **851**, 143 (2017).

24. Qu, Y. & Zhang, B. Magnetic Interactions in White Dwarf Binaries as Mechanism for Long-period Radio Transients. *ApJ* **981**, 34 (2025).
25. Buckley, D., Meintjes, P., Potter, S., Marsh, T. & Gänsicke, B. Polarimetric evidence of a white dwarf pulsar in the binary system ar scorpii. *Nature Astronomy* **1**, 0029 (2017).
26. Du Plessis, L., Wadiasingh, Z., Venter, C. & Harding, A. K. Constraining the emission geometry and mass of the white dwarf pulsar ar sco using the rotating vector model. *The Astrophysical Journal* **887**, 44 (2019).
27. Lee, Y. W. J. *et al.* The emission of interpulses by a 6.45-h-period coherent radio transient. *Nature Astronomy* **9**, 393–405 (2025).
28. Samuel J. McSweeney *et al.* Confirmation of J1755–2527 as a long period radio transient (in prep).
29. Caleb, M. *et al.* An emission-state-switching radio transient with a 54-minute period. *Nature Astronomy* **8**, 1159–1168 (2024).
30. Dong, F. A. *et al.* The discovery of a nearby 421 s transient with chime/frb/pulsar (2024).
31. Hotan, A. W. *et al.* Australian square kilometre array pathfinder: I. system description. *Publ. Astron. Soc. Aust.* **38**, e009 (2021).
32. Jonas, J. & MeerKAT Team. The MeerKAT Radio Telescope. In *MeerKAT Science: On the Pathway to the SKA*, 1 (2016).

33. Perley, R. A., Chandler, C. J., Butler, B. J. & Wrobel, J. M. The Expanded Very Large Array: A New Telescope for New Science. *ApJ* **739**, L1 (2011).
34. Perley, R. A. & Butler, B. J. An accurate flux density scale from 50 mhz to 50 ghz. *The Astrophysical Journal Supplement Series* **230**, 7 (2017).
35. Perley, R., Greisen, E. & Hugo, B. EVLA Memo 219 Enabling MeerKAT Polarimetric Imaging in AIPS. Tech. Rep., National Radio Astronomy Observatory (2022).
36. Offringa, A. R. *et al.* WSCLEAN: an implementation of a fast, generic wide-field imager for radio astronomy. *Mon. Not. R. Astron. Soc.* **444**, 606–619 (2014).
37. Pritchard, J. askap-vast/dstools: v1.0.0 (2024).
38. Foreman-Mackey, D., Hogg, D. W., Lang, D. & Goodman, J. emcee: The MCMC Hammer. *PASP* **125**, 306 (2013).

Methods

Data To obtain a contiguous 36-hour track of GPM J1839–10, we employed three telescopes: the Australian Square Kilometre Array Pathfinder (ASKAP; ³¹), the MeerKAT telescope ³² in South Africa, and the Karl G. Jansky Very Large Array (VLA ³³) in the United States of America. To maximise S/N for this steep-spectrum source, we used the lowest-frequency bands available for each telescope. Details are shown in [Table 1](#).

For ASKAP and MeerKAT we used the standard observatory flagging and calibration. The

Start	End	Telescope	Frequency (MHz)	Observation ID	Proposal/Project ID
2024-08-02					
09:30	18:30	ASKAP	800–1087	SB64328	AS113
15:25	19:54	MeerKAT	544–1088	1722610713	SCI-20230907-NH-01
2024-08-03					
21:24	01:31	MeerKAT	544–1088	1722632983	SCI-20230907-NH-01
2024-08-03					
01:10	08:55	VLA	1000–2000	46270340	24A-493
09:00	17:00	ASKAP	800–1087	SB64345	AS113
15:36	21:14	MeerKAT	544–1088	1722697769	SCI-20230907-NH-01
2024-08-04					
22:12	01:33	MeerKAT	544–1088	1722722073	SCI-20230907-NH-01

Table 1: Observing details for the campaign tracking GPMJ1839–10, in chronological order. Dates and times are on a UTC scale. “Start” refers to the first sample on target and “end” refers to the last (i.e. calibration scans are omitted).

VLA data were flagged for obvious RFI and calibrated in AIPS. The flux density scale was based on the values determined for 3C286 (J1331+3030)³⁴. The EVPA values are based on the modified values for 3C286, as reported in EVLA Memo 219³⁵. We imaged all data using WSCLEAN³⁶, masking GPMJ1839–10 itself, forming a deep model of the sky for each observation. After subtracting this from the visibilities, we phase-rotated to GPMJ1839–10. Using DSTOOLS³⁷ we averaged the baseline data, using the standard conventions to convert from instrumental to celestial Stokes, producing a dynamic spectrum for each observation.

J1912–44 was observed at L-band by MeerKAT under project code DDT-20220620-PW-01 on 2022-06-26, and originally published by². It was tracked for 16 30-min scans at 208.984-kHz/2-s correlator resolution. We used the provided observatory calibration and re-imaged the data using WSCLEAN, masking J1912–44 to form a deep model of the sky. After subtracting this model, we averaged the baselines to form dynamic spectra of the pulses, then across the frequency axis to produce light curves. (Dispersion is negligible across this band.)

Light curve generation The flux densities S_ν of each frequency channel of the dynamic spectra were scaled to the 1 GHz flux density $S_{1\text{GHz}}$ predicted by the spectral fit previously published⁴.

The spectral model is of the form

$$S_\nu = S_{1\text{GHz}} \left(\frac{\nu}{1\text{GHz}} \right)^\alpha \exp q \left(\log \frac{\nu}{1\text{GHz}} \right)^2 \quad (1)$$

with $\alpha = -3.17 \pm 0.06$ and $q = -0.56 \pm 0.03$. The shape of the spectrum was not found to vary within uncertainty as either a function of orbital or spin phase. The dynamic spectra were then de-dispersed by $\text{DM} = 273.5 \pm 2.5 \text{ pc cm}^{-3}$ and averaged over frequency to produce the light curves.

The stokes Q and U components were corrected for rotation measure by $RM = 531.83 \pm 0.14$ rad m^2 , which was also not found to vary. Barycentric correction was applied to the time axis using the DE430 ephemeris for the Solar System barycentre, and the MeerKAT PA was corrected for the parallactic angle.

Timing analysis The GPMJ1839–10 spin period $P_A = 1318.1957 \pm 0.0002$ s was calculated from the previously reported $P_B = 1265.2197 \pm 0.0002$ s as the spin-orbit beat period using

$$P_B = \frac{T}{T/P_A + 1}. \quad (2)$$

To measure the orbital period, the sparseness of the data and the nature of the periodicity makes standard techniques like Fourier analysis and phase dispersion measure unreliable. [Figure 4](#) shows all pulses detected of GPMJ1839–10 folded on the orbital period, including those found in historical data, with the oldest detection in 1988. See [4](#) for details of the historical detections. The y axis is the number of orbits since the most recent detection on UTC 09/11/2024 06:17:30, and the x axis is the residual, with orbital phase 0 chosen to be between the two pulse groups. The orbital envelope width is measured from the leftmost pulse edge to the rightmost pulse edge. If we assume that the historical pulses arrived in the same range of orbital phase as the recent pulses, then for a convincing timing solution all pulses should lie in a central ~ 12000 s column on [Figure 4](#).

Pulses were determined to be the regions of the light curves for which flux > 10 mJy and flux $> 6 \times$ RMS. The RMS of lightcurves was calculated only for the regions of the lightcurves for which flux < 10 mJy to avoid including the pulses in the noise measurement. Trial periods

were searched in steps of 0.01 s, and for each period the envelope width is shown in [Figure 4](#). Envelope widths greater than half of the period are meaningless since the measurement depends on the choice of phase centre. There is only one minimum envelope width less than half the period at $T = 31482.4 \pm 0.2$ s. the period uncertainty is the width of the plateau at the minimum in the zoomed cutout. The uncertainty bars are the residual uncertainties given the uncertainty in period. All trial periods outside of the uncertainty range result in some of the historical pulses outside of the envelope of the most recent observations.

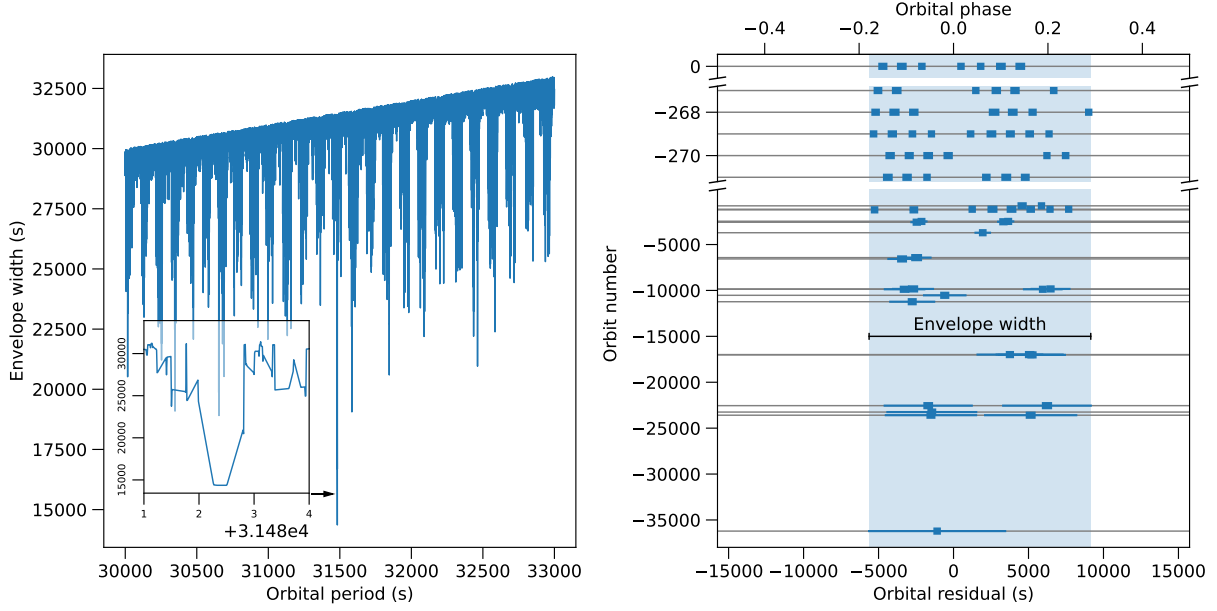


Figure 4: Left: Envelope width for trial orbital periods. Right: Detected pulses folded on the orbital period. The y axis is the orbital period number since the most recent detection (negative means backward in time). The widths of the blue rectangles are the pulse widths. The blue lines are the uncertainties in residual given the uncertainty in period. The envelope width is measured from the leftmost pulse edge to the rightmost pulse edge.

Geometric model The unit vector of the WD magnetic moment in Cartesian coordinates is

$$\hat{\mu} = (\cos \phi \sin \alpha, \sin \phi \sin \alpha, \cos \alpha) \quad (3)$$

The unit vector from the origin to the MD is

$$\hat{r}_{\text{MD}} = (\cos i \cos \phi_{\text{orb}}, \sin \phi_{\text{orb}}, -\sin i \cos \phi_{\text{orb}}) \quad (4)$$

The unit vector from the origin to the Earth is

$$\hat{r}_E = (\sin \zeta \cos \phi_0, \sin \zeta \sin \phi_0, \cos \zeta) \quad (5)$$

The angle β_{MD} between the MD and the WD beam is then

$$\hat{\mu} \cdot \hat{r}_{\text{MD}} = \cos \beta_{\text{MD}} \quad (6)$$

$$\beta_{\text{MD}}(\phi_{\text{orb}}, \phi) = \arccos(\cos \phi \sin \alpha \cos i \cos \phi_{\text{orb}} + \sin \phi \sin \alpha \sin \phi_{\text{orb}} - \cos \alpha \sin i \cos \phi_{\text{orb}})$$

and the angle β between the Earth and the WD beam is

$$\hat{r}_E \cdot \hat{\mu} = \cos \beta \quad (7)$$

$$\beta(\phi) = \arccos(\sin \zeta \sin \alpha \cos(\phi_0 - \phi) + \cos \zeta \cos \alpha)$$

We assume that the radio beam has a Gaussian cross-section. This shape of course cannot reproduce the intricate structure, but given the variability a simple shape was decided to be the best approximation. We set the Gaussian's standard deviation to be $1/5^{\text{th}}$ of the full beam width W_{spin} .

Then, the fractional intensity observed on Earth is

$$f_{\text{spin}}(\beta) = \exp \frac{-\beta^2}{2(W_{\text{spin}}/5)^2} \quad (8)$$

where W_{spin} is the opening angle in radians. We also assume that the interaction with the MD modulates the intensity with a Gaussian profile with a maximum at $\beta_{\text{MD}} = 0$ when the beam is pointed towards the MD. The orbital modulation function is

$$f_{\text{orb}}(\beta_{\text{MD}}) = \exp \frac{-\beta_{\text{MD}}^2}{2(W_{\text{orb}}/5)^2} \quad (9)$$

The predicted intensity I_{pred} observed on Earth is the product $f_{\text{spin}}(\beta)f_{\text{orb}}(\beta_{\text{MD}})$, but to account for either pole producing emission we add the same product offset by π radians. Thus,

$$I_{\text{pred}}(\beta, \beta_{\text{MD}}) = C[f_{\text{spin}}(\beta)f_{\text{orb}}(\beta_{\text{MD}}) + f_{\text{spin}}(\beta - \pi)f_{\text{orb}}(\beta_{\text{MD}} - \pi)] \quad (10)$$

where C is a coefficient with units of Jy.

Model fitting We used the ensemble Markov chain Monte Carlo (MCMC) sampler `emcee`³⁸. We

define the likelihood P_{fit} that the model fits the data as

$$\ln P_{\text{fit}} = -\frac{1}{2} \sum_{k=1}^N \left[\left(\frac{I_{\text{obs}}^{(k)} - I_{\text{pred}}^{(k)}}{\sigma_k} \right)^2 + \ln(2\pi\sigma_k^2) \right] \quad (11)$$

where N is the number of data points, $I_{\text{obs}}^{(k)}$ and $I_{\text{pred}}^{(k)}$ are the observed and predicted intensities for the k^{th} data point respectively, and σ_k is the k^{th} uncertainty. The angles $\phi_{\text{orb}}^{(k)}$ and $\phi^{(k)}$ were calculated for each data point using the timing residuals τ for the spin and orbital periods

$$\tau(t, p) = t - t_0 - \left[\frac{t - t_0}{p} + \frac{1}{2} \right] p \quad (12)$$

where p is the respective period and t_0 is the reference time. Then,

$$\phi_{\text{orb}}^{(k)} = \frac{2\pi}{T} \tau(t_k, T) + \phi_{\text{orb}}^{(0)} \quad (13)$$

$$\phi^{(k)} = \frac{2\pi}{P} \tau(t_k, P) + \phi^{(0)} \quad (14)$$

where $\phi_{\text{orb}}^{(0)}$ and $\phi^{(0)}$ are the ϕ_{orb} and ϕ angles at the reference time t_0 .

The beam and modulation widths W_{spin} and W_{orb} were not fit using MCMC because it tended to find unreasonable local P_{fit} maxima (such as $W_{\text{spin}} = W_{\text{orb}} = 0$) because the real pulse profiles are so non-Gaussian. Rather than an explicit description of the beam profile, the Gaussian functions may be thought of as a weighting for how well the predicted pulse region on the spin-orbit dynamic pulse profile agrees with the region where pulses were observed. Instead of fitting the widths, we calculate the minimum W_{spin} and W_{orb} such that all observed pulses would be observable given the

other parameters:

$$W_{\text{spin}} = \max_{k \in J} \{ \beta(\phi^{(k)}) \} \quad (15)$$

$$W_{\text{orb}} = \min_{k \in J} \{ \beta_{\text{MD}}(\phi_{\text{orb}}^{(k)}, \phi^{(k)}) \} \quad (16)$$

where J is the set of data indices which contain pulses according to the conditions in [Timing analysis](#). The coefficient C was also not fit using MCMC because it can be simply calculated analytically by solving for the roots of the derivative of [Equation 11](#) which gives

$$C = \frac{\sum_{k=1}^N I_{\text{pred}^*}^{(k)} I_{\text{obs}}^{(k)} / \sigma_k^2}{\sum_{k=1}^N \left(I_{\text{pred}^*}^{(k)} / \sigma_k \right)^2} \quad (17)$$

where $I_{\text{pred}^*} = I_{\text{pred}}/C$. This way, the model parameters are reduced to 6 $(\phi_{\text{orb}}^{(0)}, \phi^{(0)}, i, \alpha, \phi_0, \zeta)$, and the parameter space is quite stable as shown by [Figure 5](#).

[Figure 5](#) is a corner plot for the fitting of GPM J1839–10 folded on P_B . There is a linear relationship between i and α , but their range is limited by the other parameters. This degeneracy becomes significant if there is only one pulse group, such as for J1912–44. If we choose instead P_A as the spin period, no good fit can be found because it is impossible for this model to predict a dynamic pulse profile where two pulse groups are on top of each other. We also tried other beat periods, and only P_B produces a good fit. This makes us confident that P_B is the spin period. It should be noted that reflections along \hat{x} and/or \hat{z} lead to identical dynamic pulse profiles, so those transformations can be applied to get more pleasing angles.

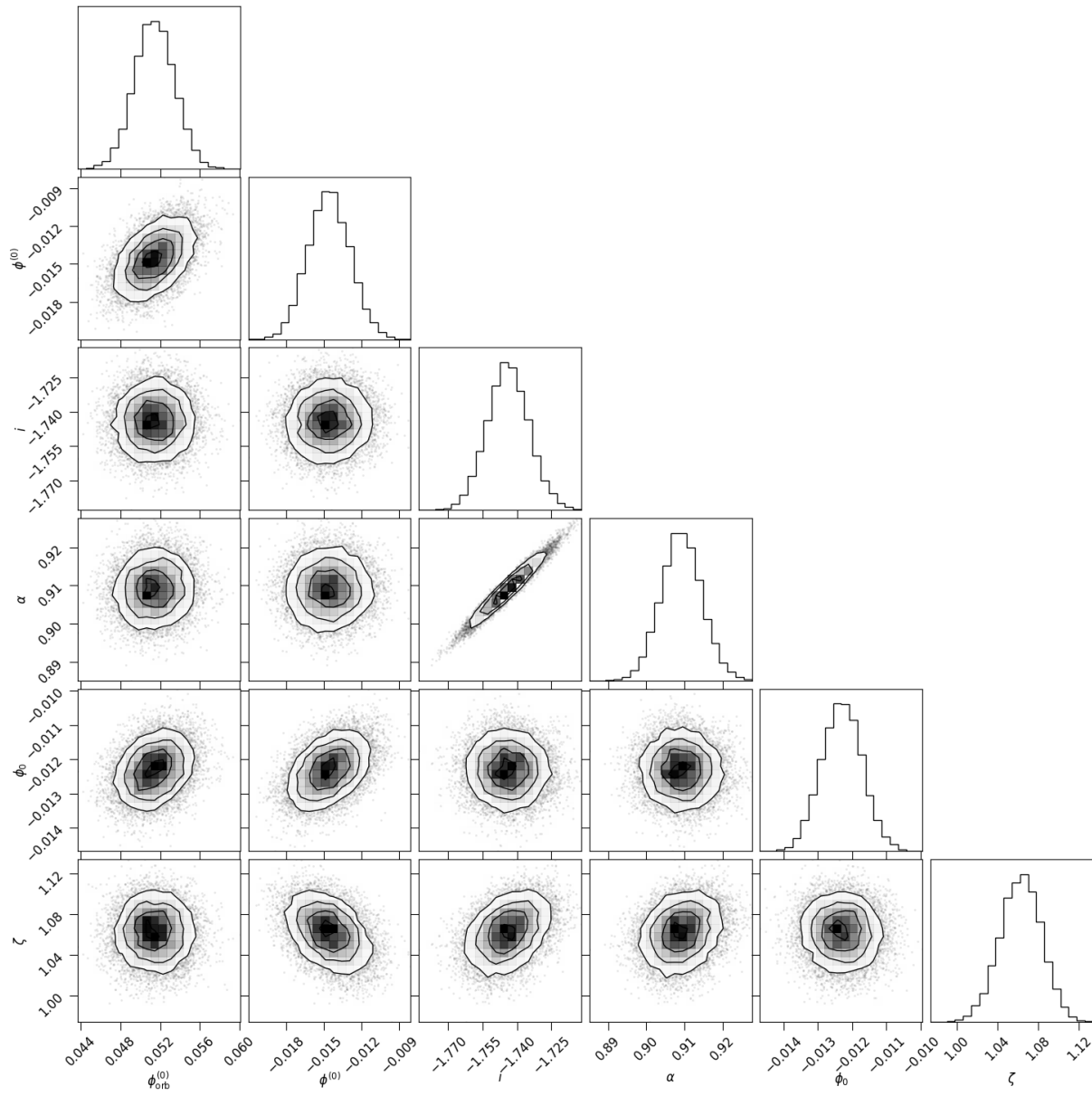


Figure 5: MCMC corner plot for GPMJ1839–10. The axis units are radians.

	Variable	Value
Priors	P	1265.2197 ± 0.0002 s
	T	31482.4 ± 0.2 s
	M_{WD}	[0.600, 1.200] M_{\odot}
	M_{MD}	[0.140, 0.500] M_{\odot}
Fitted	i	100.1 ± 0.6 °
	α	52.1 ± 0.4 °
	ϕ_0	179.29 ± 0.04 °
	ζ	61 ± 2 °
	W_{spin}	65 ± 3 °
	W_{orb}	70 ± 1 °
Calculated	A	[1.934, 2.551] R_{\odot}
	R_{MD}	[0.207, 0.574] R_{\odot}
	R_c	[0.212, 0.267] R_{\odot}
	R_{rl}	[0.513, 0.784] R_{\odot}
	R_{lc}	86.29970 ± 0.00002 R_{\odot}
	R_A	[0.187, 0.828] R_{\odot}

Table 2: Table of results for GPM J1839–10. Top are priors for the MCMC fit and calculations. Middle are the results of the MCMC fit, with the uncertainties being the 1σ credible intervals. Bottom are results which do not depend on the fitted geometry.

	Variable	Value
Priors	P	319.3490 ± 0.0001 s
	T	14525.5588 ± 0.0001 s
	i	[53, 65] °
Fitted	α	[42, 70] °
	ϕ_0	[-48, -17] °
	ζ	[39, 73] °
	W_{spin}	[20, 60] °
	W_{orb}	[67, 90] °

Table 3: Table of results for J1912–44. Top are priors for the MCMC fit and calculations. Middle are the results of the MCMC fit, with the uncertainties being the 1σ credible intervals.

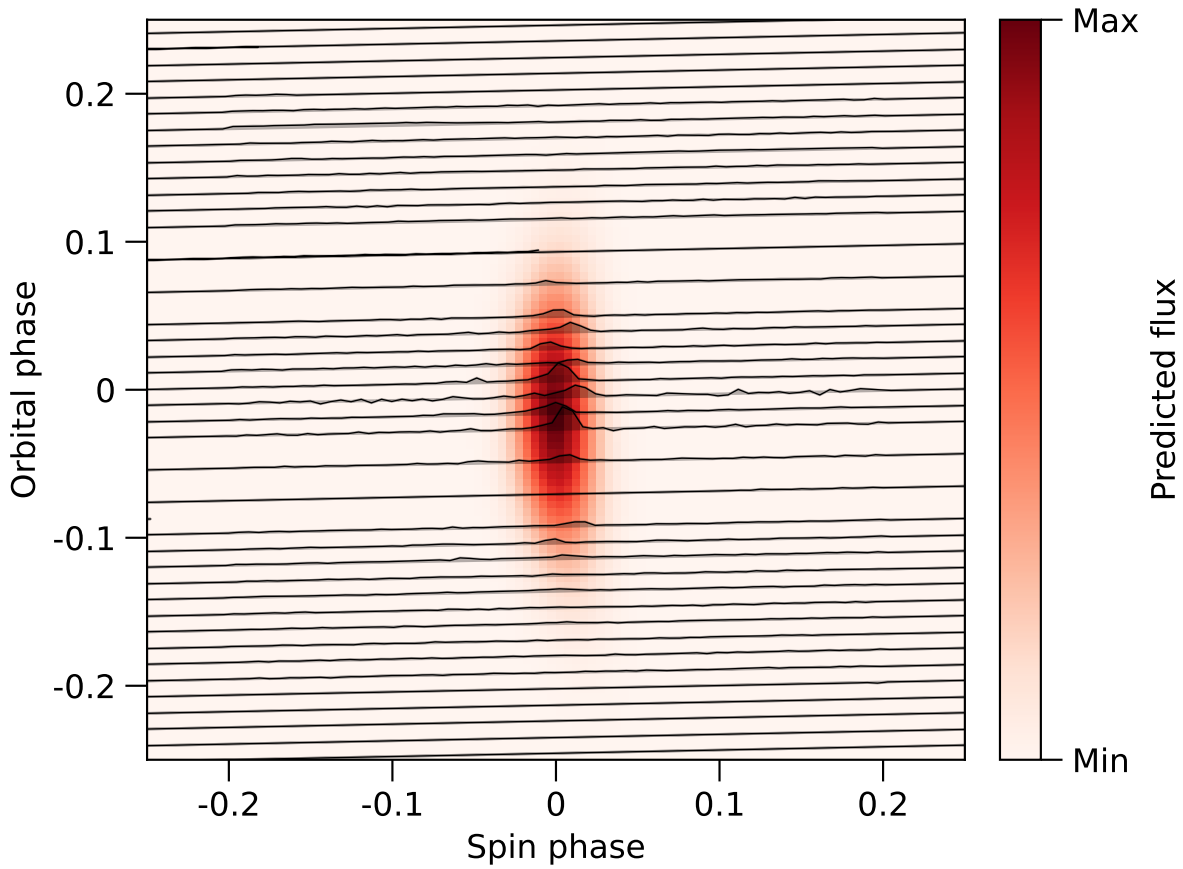


Figure 6: Modelled dynamic pulse profile for J1912–44.

Alternative geometries The three panels of [Figure 7](#) are alternative interpretations of the geometry which we investigated but ultimately rejected.

- a. What if the emission is not in the direction of the WD magnetic moment, and the observed flux density is purely a function of β_{MD} , the angle between the WD magnetic moment and the MD? While the predicted pulse group pattern does resemble the observations, no better

fit is possible than pictured. This means the emission must be beamed in (or close to) the direction of the WD pole.

- b. What if the two pulse groups are from opposite poles of the WD? The two pulse groups must be separated by ~ 0.5 spin phase, so this interpretation was discarded.
- c. What if the emission is 180° bi-directional, regardless of which WD pole sweeps the MD? In this case, we should see emission around orbital phases 0.0 and 0.5, which requires doubling the orbital period to ~ 18 hours. Although the predicted placement of the pulse groups is correct, there is no qualitative difference between the observed pulses at opposite orbital phases in either total flux density, polarised flux density, or position angle. We therefore favour the ~ 9 hour orbit.

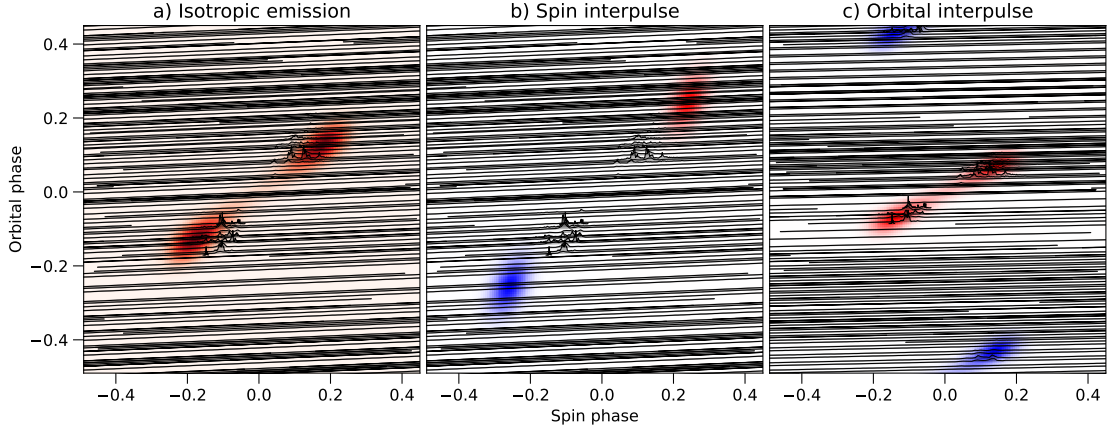


Figure 7: Best fits for alternative configurations. White indicates no predicted emission, and red or blue indicate emission from different sources. a) The emission is isotropic. b) The two pulse groups originate from opposite WD poles, indicated by red and blue. c) The emission is 180° bi-directional, regardless of which pole sweeps across the MD. In this case, the orbital period is doubled. Red and blue indicates whether the WD is behind or in front of the MD.

Other calculations Using a range of MD masses of $M_{\text{MD}} \in [0.14, 0.5]M_\odot$ and a range of WD masses of $M_{\text{WD}} \in [0.6, 1.2]M_\odot$, the orbital separation A assuming a circular orbit is

$$A = \left(\frac{G(M_{\text{MD}} + M_{\text{WD}})T^2}{4\pi^2} \right)^{\frac{1}{3}} \in [1.93, 2.55]R_\odot \quad (18)$$

Approximating the Roche lobe as a sphere, its radius R_{rl} is

$$R_{rl} = A(0.46224) \left(\frac{q}{1+q} \right)^{\frac{1}{3}} \in [0.513, 0.784]R_\odot \quad (19)$$

where $q = M_{\text{MD}}/M_{\text{WD}}$. Assuming an MD stellar radius R_{MD} of

$$R_{\text{MD}} = \left(\frac{M_{\text{MD}}}{M_\odot} \right)^{0.8} R_\odot \in [0.207, 0.574]R_\odot \quad (20)$$

the Roche lobe cannot be filled, therefore the system is not accreting. This is consistent with the lack of x-ray emission detected ⁴.

The light cylinder radius R_{lc} is the radius at which the angular velocity of the WD matches the speed of light. We find

$$R_{lc} = \frac{cP}{2\pi} = 86.29970 \pm 0.00001 R_{\odot} \quad (21)$$

The corotation radius R_c is the radius at which the orbital period is equal to the spin period. Using [Equation 18](#) we get

$$R_c = \left(\frac{G(M_{\text{MD}} + M_{\text{WD}})P^2}{4\pi^2} \right)^{\frac{1}{3}} \in [0.212, 0.267] R_{\odot} \quad (22)$$

To calculate the Alfvén radius R_A we assume $\dot{M}_{\text{WD}} = 10^{-14} M_{\odot} \text{ yr}^{-1}$ for a solar-like star ¹⁸. Then,

$$R_A = \left(\frac{2R^6 B_p^2}{2\dot{M}_{\text{MD}} \sqrt{GM_{\text{WD}}}} \right)^{2/7} \in [0.187, 0.828] R_{\odot} \quad (23)$$

The distance A_{WD} of the WD from the centre of mass around which the system rotates is

$$A_{\text{WD}} = \frac{AM_{\text{MD}}}{M_{\text{MD}} + M_{\text{WD}}} \in [0.246, 1.003] R_{\odot} \quad (24)$$

The maximum difference in light travel time Δt from the WD between opposite orbital phases is

$$\Delta t = 2 \frac{A_{\text{WD}}}{c} \in [1.15, 4.68] s \quad (25)$$

where c is the speed of light. The maximum possible time delay in our model is much smaller because we do not view the orbital plane edge-on. We did not correct the timing residuals for this delay because it is of the scale of our time resolution and insignificant compared with the intrinsic arrival time variability of the source.

In the neutron star pulsar case the emission site is bounded by the last open field lines of the dipolar magnetic field of the WD at the emission site at distance r_{em} from the WD. Assuming that the emission site is within the orbital radius, $r_{em} \leq A \leq 2.55R_{\odot}$, the angle θ between $\vec{\mu}$ and the emission site boundary is

$$\theta = \arcsin \sqrt{\frac{r_{em}}{R_{lc}}} \leq 9.898^{\circ} \quad (26)$$

For a dipolar magnetic field in a spherical coordinate system,

$$\vec{B} \propto 2 \cos \theta \hat{r} + \sin \theta \hat{\theta} \quad (27)$$

If the radiation at the emission site is generated tangential to the magnetic field line, then the angle ρ of \vec{B} with respect to $\vec{\mu}$ at the emission site boundary is the half-opening angle of the beam. We calculate the maximum half-opening angle using [Equation 27](#) by

$$\tan(\rho - \theta) = \frac{\sin \theta}{2 \cos \theta} = \frac{1}{2} \tan \theta \quad (28)$$

to get $\rho \leq 14.9^{\circ}$.

Acknowledgements

This research is supported by an Australian Government Research Training Program (RTP) Scholarship. N.H.-W. is the recipient of an Australian Research Council Future Fellowship (project number FT190100231). N.R. is supported by the European Research Council (ERC) via the Consolidator Grant “MAGNESIA” (No. 817661) and the Proof of Concept “DeepSpacePulse” (No. 101189496), by the Catalan grant SGR2021-01269 (PI: Graber/Rea), the Spanish grant ID2023-153099NA-I00 (PI: Coti Zelati), and by the program Unidad de Excelencia Maria de Maeztu

CEX2020-001058-M.

This scientific work uses data obtained from Inyarrimanha Ilgari Bundara, the CSIRO Murchison Radio-astronomy Observatory. We acknowledge the Wajarri Yamaji People as the Traditional Owners and native title holders of the Observatory site. CSIRO's ASKAP radio telescope is part of the Australia Telescope National Facility (<https://ror.org/05qajvd42>). Operation of ASKAP is funded by the Australian Government with support from the National Collaborative Research Infrastructure Strategy. ASKAP uses the resources of the Pawsey Supercomputing Research Centre. Establishment of ASKAP, Inyarrimanha Ilgari Bundara, the CSIRO Murchison Radio-astronomy Observatory and the Pawsey Supercomputing Research Centre are initiatives of the Australian Government, with support from the Government of Western Australia and the Science and Industry Endowment Fund.

The MeerKAT telescope is operated by the South African Radio Astronomy Observatory, which is a facility of the National Research Foundation, an agency of the Department of Science and Innovation. The National Radio Astronomy Observatory is a facility of the National Science Foundation operated under cooperative agreement by Associated Universities, Inc.

We acknowledge Ben Stappers, Ewan Barr, and Yunpeng Men for contributing to the MeerKAT proposal. We acknowledge Scott Hyman, Tracy Clarke, and Simona Giacintucci for contributing to the VLA proposal. We thank Ingrid Pelisoli and Simone Scaringi for useful discussions on white dwarf evolution.

Author contributions

Cs.H performed the orbital timing, spin/beat period analysis, polarisation analysis, developed the geometric model, and contributed to the discussion in the manuscript. N.R contributed to the formulation of the model and its physical interpretation, and contributed to the discussion in the manuscript. N.H.-W led the proposals for the radio data toward GPM J1839–10, imaged and produced dynamic spectra from the radio data used in this work, and contributed to the formulation of the model and discussion in the manuscript. S.M contributed to the formulation of the model, and contributed to the discussion in the manuscript. R.P generated the observing scripts and calibrated the data for the VLA observations. E.L processed the ASKAP data and contributed to the polarisation analysis.

Competing interests

The authors declare no competing interests.

Data availability

Data supporting the findings of this study are available from the corresponding author upon request.

Code availability

The code used for the geometric model and MCMC fitting is available at

<https://github.com/CsanadHorvath/GeometricLPT.git>.

An interactive web visualisation is available at

<https://www.desmos.com/3d/6bisspujwe>.